Matrix stiffness and blood pressure together regulate vascular smooth muscle cell phenotype switching and cofilin dependent podosome formation

Brian Sit[1,2,3*], Zhen Feng[3*], Ioannis Xanthis[1], Emilie Marhuenda[1], Simona Zingaro[2], Cathy Shanahan[4], Gareth E Jones[2], Cheng-han Yu[3,‡] and Thomas Iskratsch[1,2,‡]

1 School of Engineering and Materials Science, Queen Mary University of London, London, UK
2 Randall Centre for Cell and Molecular Biophysics, King's College London, London, UK
3 School of Biomedical Sciences, Hong Kong University, Hong Kong
4 School of Cardiovascular Medicine and Sciences, King's College London, London, UK
* Authors contributed equally
‡ Correspondence:
Thomas Iskratsch: t.iskratsch@qmul.ac.uk
Cheng-han Yu: chyu1@hku.hk

Abstract
Vascular smooth muscle cells (VSMCs) play a central role in the onset and progression of atherosclerosis. In pre-atherosclerotic lesions, VSMCs switch from a contractile to a synthetic phenotype and subsequently remodel the microenvironment, leading to further disease progression. Ageing and associated mechanical changes of the extracellular matrix as well as hypertension are major risk of atherosclerosis. Consequently, we sought here to systematically study the impact of mechanical and chemical stimulations on VSMC phenotypic switching. We find that the hemodynamic pressure and matrix stiffness have overlapping effects and together contribute to the phenotypic changes in cellular mechanics, podosome formation, and matrix degradation. We further identify cofilin as a key modulator of the mechanosensitive phenotype switch, which is regulated through Ca^{2+}/slingshot-dependent pressure sensing and RhoA/ROCK-dependent stiffness sensing pathways. Altogether, microenvironment stimulations of high pressure and soft matrix collectively promote the cofilin activity, VSMC migration, and the early progression of atherosclerosis.

[148 words]

Introduction

Cardiovascular diseases are the primary cause of mortality worldwide. Vascular ageing is dramatically increasing the risk of cardiovascular disease, including systolic hypertension, coronary artery disease, stroke, heart failure and atrial fibrillation or atherosclerosis[1-5]. This ageing process is related to both chemical/molecular as well as mechanical changes, including changes to the blood flow (wall stress, haemodynamic pressure) and stiffness of the arterial wall. Endothelial cells (ECs) sense the wall stress and shear direction, and the associated mechanosignalling defines atheroprone or atheroprotective regions[6]. The shear stress deforms the apical surface of ECs and is sensed amongst others by the glycocalyx, mechanosensitive ion channels and various receptors including PECAM-1, plexin D1, and integrins[6-10]. ECs communicate this then further to the underlying arterial layers and the residing vascular smooth muscle cells (VSMCs), through the extracellular matrix, growth factor signalling and direct receptor interaction[11].

VSMCs are necessary for matrix formation and contractility of the arterial wall but can adopt alternative phenotypes in response to chemical and physical signals. The phenotypically altered cells have been described as synthetic, macrophage-like, or foam cells[12, 13]. Previous studies on the involvement of VSMCs in atherosclerosis have largely focused on their role in advanced atherosclerotic processes i.e., fibrous cap formation and plaque stability or rupture. However recent research increasingly points to a critical role for VSMCs in the initiation and early phases of atherosclerosis, including diffuse intimal thickenings (DIT) - the most likely precursor of pre-atherosclerotic plaques[12, 14], as well as pathological intimal thickening (PIT), which is considered the first stage of atherosclerosis[12]. Moreover, lineage tracing data shed light into origin of the atherosclerotic VSMCs and identified that there is no widespread migration/invasion from the media layer, but that the VSMC within the intima layer change their phenotype to define the disease onset and progression[12, 15, 16]. In DITs, VSMCs are considered the major source of extracellular matrix proteins and especially proteoglycans (versican, biglycan, and perlecan, as well as others to a lesser degree)[17] in the arterial wall, hence leading to the thickening of the intima and the progression to PIT[12, 18]. This progression is promoted by retention of apolipoproteins, oxidation of lipids, VSMC phenotypic switching, proliferation and apoptosis. Again, the capability of (phenotypically altered) VSMCs to secrete and remodel the extracellular matrix is critical for this step[19-22].

In addition to the role of EC-VSMC cross-signalling, there is circumstantial evidence suggesting that mechanical forces also direct impact on the VSMC phenotype. DIT has long been considered an adaptation to blood flow[23]. Moreover, mechanical strain altered mRNA expression and accumulation of extracellular matrix proteins from VSMCs[22]. Finally, pressure induced phenotypic changes and migration in VSMCs[24, 25] - although these studies used static pressure and rigid tissue culture plastic and therefore non-physiological stimuli. In comparison, the intima layer is relatively compliant compared to the stiffer underlying media and adventia layers or the internal elastic lamina and the hemodynamic pressure results therefore in both cyclic stretch and compression of the intima and the residing VSMCs[26-31]; i.e. ECG measurements demonstrate a stronger reduction in intima thickness than can be explained by stretching alone, suggesting a compression as a result of a comparatively small elastic modulus of the intima compared to the underlying layers[26]. The relative compression amounts to ~ 1.5% in young (<50 years) and 2.7 and 4.7% in old (>50 years) women and men, respectively, suggesting changes to blood pressure and mechanical properties during ageing affect the mechanical stimuli VSMCs will be exposed to[26].

Arteries are composite structures with complex mechanical behaviour, which importantly differs between macro and microscale[32, 33]. The macroscale values are in the range of hundreds of kilopascals to megapascals, with a trend from low stiffness in childhood to higher values in old age due to fracture of elastin, increase in collagen and calcium deposits[32-

[37]. The increasing macroscale stiffness of the artery has a direct effect on increased systolic blood pressure and pulse pressure, thereby leading to deleterious cardiovascular outcomes with hypertension being a main driver for atherosclerosis[38].
In contrast, microscale values, important for cellular mechanosensing and transduction are magnitudes lower.
The Young's modulus of the endothelial layer was reported to be within the range of 0.32-5kPa[39-44]. The elastic moduli of the tunica intima and media are around 15-50kPa[27, 28] and 29-190kPa[28-31], respectively whereby the discrepancy between individual studies is likely a result of different compositions in different arteries, different model systems, different age of animals and different techniques. Measurements of the fibrotic plaques give an indication of the intima stiffness during DIT and PIT where the non-collagenous matrix increases[12, 18]. These suggest a relative compliant environment. Cellular fibrotic regions have a young's modulus of 1.6 to 25kPa, while young's moduli between 0.6 and 13.7 kPa have been measured in lipid rich regions[45].
Because hypertension is a major risk factor for atherosclerosis and because of the differences in elastic moduli between different arterial layers that contain VSMCs (media vs intima vs pre-atherosclerotic lesions or atherosclerotic plaques), we wanted here to study the combined effect of matrix and hydrodynamic pressure (mimicking normal and hypertensive blood pressure) on vascular smooth muscle cell phenotypes.
Combining surfaces with defined stiffness and hydrodynamic pressure stimulation we find overlapping effects of the different mechanical stimuli that favour a phenotypic switch, demarcated by large-scale changes to cell morphology and actin organisation, and especially formation of matrix degrading podosomes. We further study the regulation of the podosomes downstream of mechanical signals and the molecular pathways, identifying cofilin as a key regulator of VSMC podosome mechanosensing. Together our data highlights the strong contribution of different mechanical factors on VSMCs during the onset and progression of atherosclerosis.

Results

The phenotypic switch of vascular smooth muscle cells is regulated through haemodynamic pressure and matrix stiffness

Vascular smooth muscle cells (VSMCs) play a key role in various stages of atherosclerosis and disease progression is associated with phenotypic switching. Here we wanted to study the combined effect of matrix stiffness and hemodynamic pressure on vascular smooth muscle cell phenotype. Specifically, we plated A7r5 VSMCs onto PDMS coated coverslips with defined stiffness, mimicking the stiffness range of the media layer (130kPa), the intima layer (20kPa) as well as lipid rich areas of atherosclerotic plaques or pre-atherosclerotic lesions (1kPa). In addition, the VSMCs on the stiffness-defined substrates were subjected to hydrodynamic pressure stimulation, mimicking either healthy normal blood pressure (NBP, 60/120 mmHg) or stage II hypertension (HT, 180/120 mmHg) (Fig 1A), using a pressure stimulator (CellScale Mechanoculture TR, modified for a low-pressure range), situated inside a 37°C tissue culture incubator. Control cells were kept inside the chamber without the pressure stimulation. After 12 hours, cells were fixed and stained with phalloidin before cell segmentation and analysis of morphological parameters with CellProfiler (cell shape and F-actin shape descriptors) and the ImageJ OrientationJ plugin (F-actin alignment)[46, 47]. To detect F-actin dots, which we initially observed in some cells, we trained a pixel classification using Ilastik and measured the number and the area of dots in cells after the segmentation (Fig 1B). We then performed a dimensionality reduction using t-distributed Stochastic Neighbor Embedding (t-SNE) (Fig 1C), and two separate clusters were identified, including primary control and NBP treated cells (cluster 1) or HT treated cells (cluster 2) (Fig 1D).

Overall, we noted a correlation of the cluster composition with the pressure stimulation regime and, to a smaller degree, with the substrate stiffness (Fig 1D). Consistent with this, cell shape analysis using the visually-aided morpho-phenotyping image recognition "VAMPIRE" software[48] indicated an increase in round, compared to spindle shaped cells after the HT treatment (Fig 1E), while normal blood pressure treatment in contrast preserved spindle shapes and further resulted in an apparent increase in cellular alignment (not shown). After HT treatment, we also found a substantial change to the actin organisation, including a reduction in actin alignment and overall organisation (Fig 1F). Specifically, we also detected changes to actin dot occurrence, which occurred either as single dots or clusters (Fig 1G). VSMCs are known to assemble podosomes in response to chemical or biophysical stimuli[33]. Podosomes consist of a core of densely polymerized F-actin, surrounded by a ring complex, containing adhesion proteins. Indeed, cortactin, one of the podosome markers, localized with the F-actin core in VSMCs and was surrounded by adhesion proteins zyxin or vinculin (Fig 1G,H). Localized degradations of the gelatin matrix were also observed around the podosome (Fig 1J,K). Surprisingly, the number of podosome-forming cells showed not only a strong increase after pressure stimulation compared to the control, but also depended largely on matrix stiffness. In particular, there were more podosome-forming cells and greater gelatin degradation on the 1kPa surface, compared to 130kPa. (Fig 1I and K). The extensive changes to the cytoskeletal structures were accompanied by a reduction in the cellular stiffness, which was measured by nanoindentation with a large-diameter spherical tip placed approximately above the nucleus (Fig 1L, tip radius: 49µm, k=0.46N/m, 2µm indentation). Together these results suggest that the HT pressure globally alters the cell morphology and the actin organisation, but cells on the softer surface mimicking the stiffness of pre-atherosclerotic lesions and atherosclerotic plaques show a distinct increase in the formation of matrix-degrading podosomes.

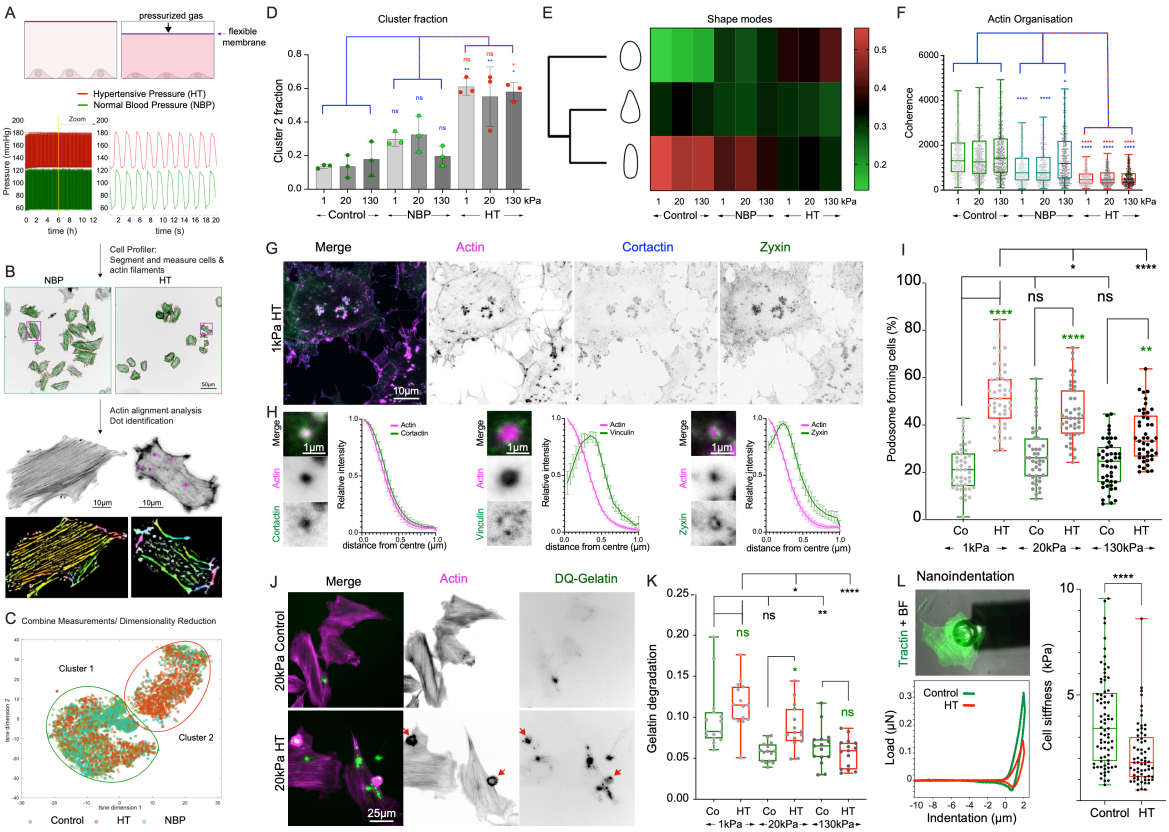

Figure 1: Hypertensive pressure, but not healthy blood pressure stimulates phenotypic switching in vascular smooth muscle cells. A) overview of the experimental protocol. Cells were plated on PDMS coated

coverslips with different stiffness (1,20,130kPa) and placed under cyclic hydrodynamic pressure mimicking either healthy (120/60mmHg) or hypertensive blood pressure (180/120mmHg), measured output from stimulator shown on left, zoom into region denoted by yellow line shown on top right. B) Cells were then fixed, stained and analysed using cell profiler for cell (middle panel, red outlines) and actin segmentation (green outlines). Segmented cells were further analysed to determine actin dots (purple outlines) or actin filament alignment (bottom panel). C) Area, shape, actin shape, orientation and actin dot measurements were combined before dimensionality reduction and cluster analysis (t-SNE) D) The presence of the various conditions in each cluster was analysed after separation of the data from the three different repeats. Error bars: SD; E) HT treatment affected shape modes of the cells. F) HT treatment resulted in reduced actin organisation (Coherence measurements using the orientationJ plugin, pooled data from three separate experiments) G) Actin dots appeared both in single dots and clusters and co-stained for cortactin, zyxin or vinculin (H), with zyxin and vinculin appearing in a ring-structure around the central actin core (H); radial profiles are normalized intensities from n=10 podosomes from 5 cells each. I) The fraction of podosome-forming cells depended on pressure and stiffness (fraction of podosome-forming cells per image with ~10-20 cells per image were counted manually from three independent experiments). J,K) Podosomes actively degraded gelatin, but the efficiency depended on stiffness and pressure (DQ-gelatin intensity over cell area, averaged per image with ~10-20 cells per image, from three independent experiments). L) the large-scale changes to the cellular cytoskeleton were also reflected by a drop in the cellular stiffness as determined by nanoindentation (data from three independent experiments). Top left: image from tractin (green) and the indenter (bright field channel). Bottom left: typical load-indentation curve for the control (green) and HT (red) treated cells. Right panel: young's moduli. *$p < 0.0332$; **$p < 0.0021$; ***$p < 0.0002$; ****$p < 0.0001$; ns, not significant; p-values from one-way ANOVA and Tukey test for multiple comparisons or t-test (L); D,F: blue asterisks are for comparison with control, red asterisks for comparison with NBP; I,K: green asterisks represent comparison to the controls of same stiffness group, black asterisks to 1kPa of same treatment group. Box plots are displayed as median, upper and lower quartile (box) and range (whiskers).

Substrate stretching is insufficient to induce the podosome formation

The haemodynamic pressure results in compression and stretching the PDMS and cells. Using nanoindentation at corresponding load, we measured approximately 12% axial compression for a 130kPa PDMS mixture (on which the number of podosome-forming cells doubled in response to HT pressure - Fig 1I), equivalent to 5.2 - 6% transverse strains with reported Poisson's ratios for PDMS mixtures between 0.43 and 0.5[49, 50] (Supplementary Fig S1A,B). Because phenotypic switching in response to pressure was more readily observed with increasing compliance, we employed a 10% cyclic biaxial stretch regime at the same frequency and duration of the pressure experiment (0.5Hz, 12h) to test if stretch alone is sufficient to induce the observed changes. After analysing the VSMCs with the same image analysis pipeline (see methods), we found however no clear differences between the cell populations (Supplementary Figure S1C,D). While we detected small but significant changes of cell shape (Supplementary Figure S1E-H), including an increase in eccentricity (more elongated shape) and form factor (more irregular shape), as well as a reduction in actin alignment, we did not detect changes in the cells ability to form podosomes (Supplementary Figure S1I). Similarly, 30 minutes static pressure application (180mmHg) stimulated podosome formation with a strong stiffness dependence, but we detected no change in the ability to form podosomes after 30 minutes static biaxial stretch (5 or 10%, Supplementary Figure S2). These results indicate that stretch alone cannot account for the phenotypic changes we observed in response to pressure and stiffness modulation.

Vascular smooth muscle podosomes are mechanosensitive after induction through chemical stimuli

In addition to the mechanical signals from the hemodynamic pressure and the extracellular matrix rigidity, VSMCs in the intima are exposed to various PKC-activating signals from the adjacent endothelial cells[11, 51-55]. Phorbol 12,13-dibutyrate (PDBu), a potent activator of PKC signalling in smooth muscle[56, 57], has been previously used to induce the formation of podosomes in VSMCs[58, 59]. Consistent with this, we found a strong induction of podosome

formation after PDBu treatment. In particular, we detected a significantly higher fraction of podosome-forming cells, as well as significant differences in the turnover and function of podosomes on the substrate with lower stiffness (Fig 2A, B). Over time, podosomes were forming and turning over only once, but frequently cyclically appearing and disappearing at the same location (fluctuating podosomes, Fig 2C,D & Supplementary Movies 1&2). Moreover, podosomes often appeared in groups whereby the formation and disappearance followed a wave-like pattern, suggesting the cross talk and time delayed coordination among the podosomes. While we did not detect an obvious correlation between such wave pattern and stiffness, we found that podosomes on the soft surfaces turned over more rapidly (Fig 2C-E) and importantly, were degrading the extracellular matrix more efficiently on soft surfaces compared to cells plated on higher stiffness (Figure 2F,G). Together these results suggest that PDBu treatment leads to highly efficient activation of podosome formation, but the stiffness-dependent behaviour persists.

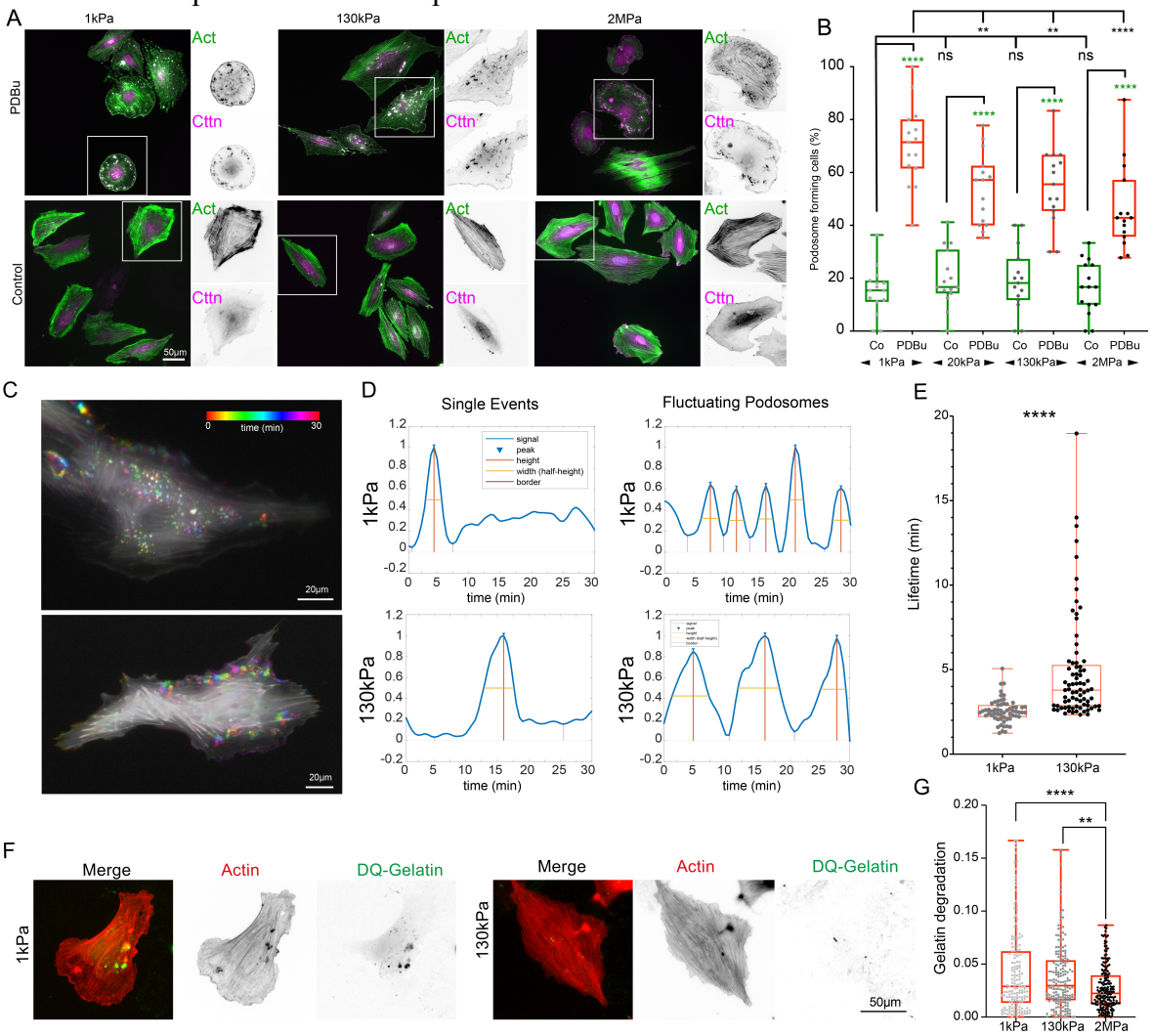

Figure 2: PDBu treatment leads to efficient podosome formation on all stiffnesses but podosome behaviour and matrix degradation are controlled by stiffness. A,B) PDBu treatment leads to stiffness dependent podosome formation. C-E) Podosomes lifetime depends on substrate stiffness. C) Colour-coded time projection of VSMC treated with PDBu on 1 and 130kPa shows dynamic podosome formation (see also Supplementary Movies 1&2). D) Podosome formation (independent of stiffness) was detected as either single event or cyclically fluctuating podosomes but showed stiffness dependence in their turnover time (measured at half-maximum of the peaks) with an increased lifetime on higher stiffness (E). F,G) Gelatin degradation (DQ-Gelatin fluorescence signal over cell area) was more extensive on compliant surfaces. *$p < 0.0332$; **$p < 0.0021$; ***$p < 0.0002$; ****$p < 0.0001$; ns, not significant; p-values from one-way ANOVA and Tukey test for multiple comparisons or t-test (E); B) green asterisks represent comparison to the controls of same stiffness

group, black asterisks to 1kPa of same treatment group. Box plots are displayed as median, upper and lower quartile (box) and range (whiskers).

Podosomal actin turnover in VSMCs is controlled by substrate stiffness

Faster turnover and recurrence of podosomes on compliant substrates suggested a stiffness dependent F-actin assembly. F-actin assembly at the podosome core is regulated through cortactin (via WASP and Arp2/3), or alternatively the actin-severing protein cofilin, which accelerates actin dynamics by generating additional barbed ends and has reported actin filament nucleation activity at high concentrations[60, 61]. Therefore, we measured both cortactin and cofilin activity by western blotting with phospho-specific antibodies. Levels of phosphorylated Y421 cortactin did not change with stiffness, however we detected a decrease in cofilin S3 phosphorylation on lower stiffnesses, suggesting a higher level of cofilin activity that was consistent with increased podosome dynamics (Fig 3A-C). Additionally, a stronger enrichment of cofilin at the podosome core was observed on softer surfaces (Fig 3D,E). To confirm the relevance of cofilin phosphorylation on podosomal actin, we transfected phospho-mimicking as well as unphosphorylatable cofilin mutants and measured the dissociation of mEOS2-actin at the podosome after spot photoswitching. Here, the presence of an active, non-phosphorylatable, cofilin mutant (S3A) increased actin turnover, while the presence of a phosphomimickinig S3E cofilin strongly reduced the turnover (Fig 3F-I). Together, these data suggest that cofilin is instrumental in regulating podosomal actin turnover downstream of extracellular matrix stiffness sensing.

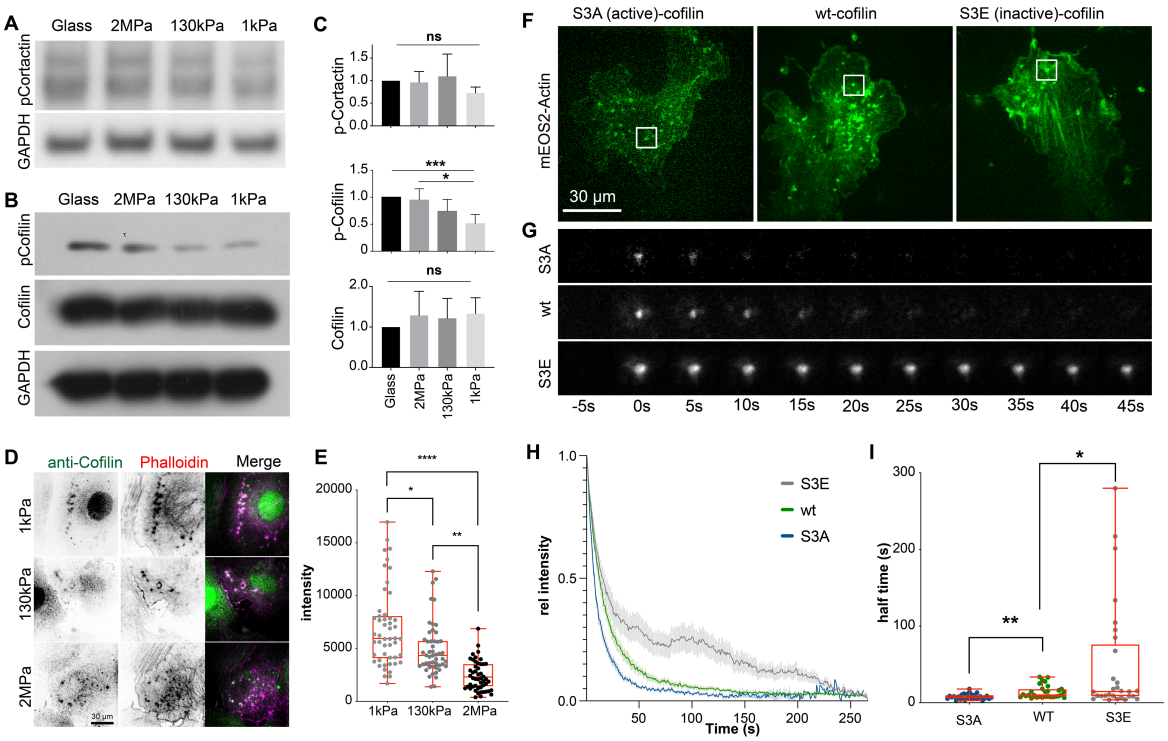

Figure 3: Cofilin localisation and activity respond to stiffness and regulate podosomal actin turnover. A-C) Cortactin phosphorylation is unaffected by stiffness, but cofilin phosphorylation is reduced on soft surfaces, indicating higher activity. Error bars: SD; D,E) Cofilin is enriched at podosomes on soft surfaces. F) Pressure stimulation leads to a reduction in cofilin phosphorylation. G-J) Transfection of phosphomimickinig or non-phosphorylatable cofilin regulates the turnover of podosomal actin. F) Cells were transfected with mEOS2-Actin and iRFP-cofilin wt, S3A (active) or S3E (inactive). G) Actin turnover was measured after photoswitching of mEOS2-Actin, indicating changes in lifetime. F-I) Fluorescence loss after photoconversion indicates slower podosomal actin turnover in presence of S3E and faster turnover in presence of S3A cofilin mutants. Plot of mean and SEM of 30 podosomes from 10 cells per condition (H) and half time (I). *$p < 0.0332$; **$p < 0.0021$;

***p < 0.0002; ****p < 0.0001; ns, not significant; p-values from one-way ANOVA and Tukey test; Box plots are displayed as median, upper and lower quartile (box) and range (whiskers).

Podosomal cofilin is regulated through RhoA, ROCK2 and LIMK2 in a stiffness-dependent manner

LIM domain kinases (LIMKs) are known to directly phosphorylate cofilin at S3 and to reduce its actin severing activity[62]. The activation of LIMK can be positively regulated by ROCK or PAK mediated phosphorylation. We sought to investigate how cofilin phosphorylation is regulated downstream of mechanical stimuli. In PDBu-stimulated VSMCs, we found that the level of phosphorylated LIMK showed the same trend as that of phosphorylated cofilin, and higher levels of phosphorylation were observed on the stiff surface (Fig 4A). Since the phospho-antibody detects both LIMK1 and LIMK2, we knocked down each isoform and found that LIMK2 was responsible for phosphorylating cofilin in A7r5 VSMCs (Fig 4B, Supplementary Figure S3 for knockdown validation). Next, we investigated the potential upstream kinases to promote the LIMK phosphorylation. We found that the activities of group 1 PAK (PAK1/2/3) and group 2 PAK (PAK4/5/6), reported by the phospho-specific antibodies, did not demonstrate any stiffness dependence. However, when ROCK1 and ROCK2 were knocked down individually, we found a strong reduction in cofilin phosphorylation after the knockdown of ROCK2, rather than ROCK1 (Fig 4A,B and Supplementary Figure S3 for knockdown validation). In agreement with the effect of the knockdowns, pan-inhibitions of Rho kinases with Y27632 (20μM) and H1152 (10μM) or ROCK2-specific inhibition with KD025 (10μM) resulted in the decrease of both cofilin and LIMK phosphorylation (Supplementary Figure S4). In addition, we found that both LIMK2 and ROCK2 were colocalised and specifically enriched at the VSMC podosome (Supplementary Figure S5). When ROCK2 and LIMK2 were individually knocked down, the transwell migration of PBDu-treated VSMCs was strongly reduced (Fig 4C). Reintroductions of ROCK2 and LIMK2 in the respective knockdown condition restored the migration capability.

Small Rho GTPase RhoA is known to act as an upstream messenger to activate ROCK-mediated signalling transductions. Indeed, we further identified higher proportions of GTP-bound RhoA when VMSCs were plated on the stiff substrate (Fig 4D). Intriguingly, using a RhoA FRET activity sensor we found high RhoA activity in areas surrounding the podosome core (Fig 4E-H, Supplementary Figure S6 and Supplementary Movie 3). Initially, the RhoA activity was reduced during the podosome assembly, as predicted by a recent study from Rafiq et al [63]. However, flashes of RhoA activity increasingly and consistently appeared in the vicinity of the podosome core during the podosome disassembly (Fig 4F-I). Apart from RhoA, Cdc42 is also reported to promote cofilin phosphorylation through PAK-mediated LIMK phosphorylation[64]. VSMCs with Cdc42-GTP inhibition by ML141 (10μM) indeed exhibited a lower level of cofilin phosphorylation, but did not show the decease phosphorylation of PAK and LIMK, suggesting a non-canonical effect of Cdc42 inhibition on cofilin (Supplementary Figure S4). Together, these results show stiffness dependent and dynamic changes to RhoA activity which regulate ROCK2 and LIMK2 mediated cofilin phosphorylation.

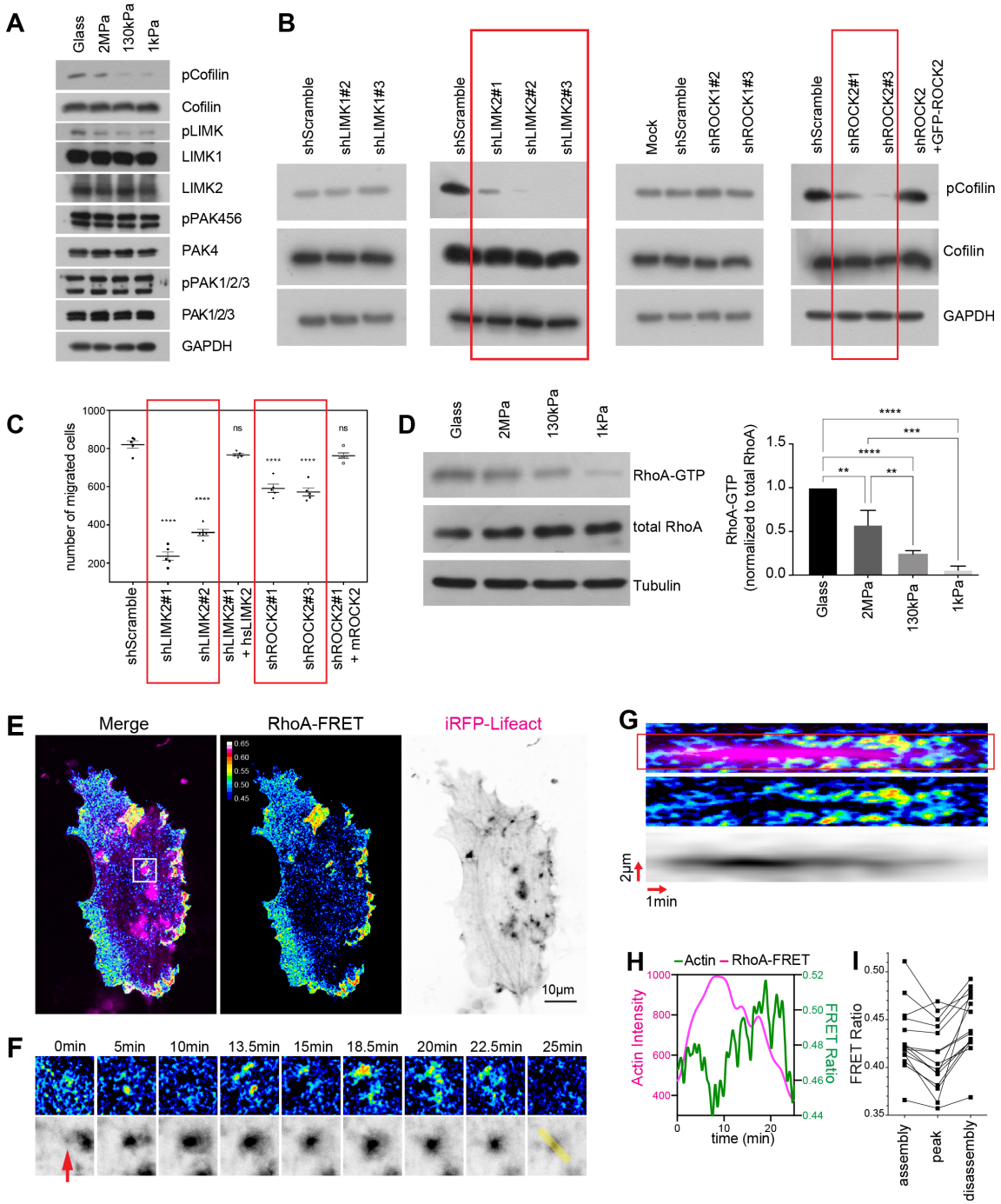

Figure 4: Rigidity sensing controls Cofilin activity through RhoA-ROCK-LIMK signalling. A) Western blot analysis of A7r5 VSMCs seeded on different stiffnesses. p-Cofilin and p-LIMK are reduced on compliant surfaces, while other antibodies do not detect stiffness dependent changes. B) LIMK2 and ROCK2 knockdown, but not LIMK1 or ROCK1 knockdown reduce p-Cofilin levels in A7r5 VSMCs (see Supplementary Fig S3 for knock down validation). C) LIMK2 and ROCK2 knockdown reduce transwell migration of VSMCs. Error bars: SEM; D) RhoA-GTP pull down assay shows a reduction in active RhoA on compliant surfaces (quantification from three independent repeats; Error bars: SD). E-G) A7r5 cells were transfected with a RhoA-FRET biosensor and iRFP lifeact to analyze the dynamic changes to RhoA activity after PDBu stimulation. CFP/YFP images were taken every 5s after donor excitation with a 445nm laser and with a dual camera setup for simultaneous acquisition (see also Supplementary Fig S6). iRFP images were taken every 100s as a reference for the podosome position. F) Time points of area outlined in white in E. G) Kymograph over line marked in yellow in F. H) Intensity profiles over time of a 3µm wide line marked by outlines in G. FRET intensity at half-max actin intensity during assembly and disassembly as well as at peak intensity from n=15 podosomes form 3 independent experiments. The iRFP image stack was filtered with a 3D gaussian filter (x=1, y=1, z=10) for

visualization purpose in panel G,H. *p < 0.0332; **p < 0.0021; ***p < 0.0002; ****p < 0.0001; ns, not significant; p-values from one-way ANOVA and Tukey test for multiple comparisons.

Pressure and PDBu stimulate cofilin dephosphorylation and podosome formation through Ca2+ and SSH

While the RhoA-ROCK-LIMK pathway clearly regulates the stiffness dependence in cofilin activity and podosome formation, it does not explain the podosome induction through hypertensive hydrodynamic pressure, suggesting an alternative mechanism. Indeed, the level of cofilin phosphorylation was decreased after cyclic HT pressure stimulation while the phosphorylation of LIMK remained unchanged (Fig 5A). Mechanosensitive channels have received wide attention as regulators of cellular behaviour since their discovery in the 1980s and especially the cardiovascular system is highly dependent on the regulation through mechanosensitive ion fluxes[10, 65, 66]. In particular, Ca^{2+} has been suggested to regulate the activity of slingshot phosphatase, which again targets cofilin[67]. Finally, PKC (activated through PDBu treatment) is not only modulated by Ca^{2+} but also affects Ca^{2+} handling[68]. Therefore, we hypothesized that hydrodynamic pressure could lead to an increase in baseline Ca^{2+} levels to induce podosome formation. When VSMCs were subject to a single indentation with a maximum pressure of 24 ± 4.4kPa (180 ± 33mmHg, Fig 5B-E), we found a consistent increase in intracellular Ca^{2+} levels, reported by the calcium indicator Cal520. Similar to pressure stimulation, PDBu treatment also resulted in a consistent increase in intracellular Ca^{2+} levels (Fig 5F,G). Noteworthy, both the pressure and the PDBu stimulation only led to a slow increase, compared to thapsigargin (TG), suggesting that both were inducing the influx of extracellular Ca^{2+} rather than the release from the intracellular calcium stores (Fig 5F,G). To examine the impact of Ca^{2+} influx on the cofilin phosphorylation, we found that the treatment with the divalent cation ionophore A23187 resulted in the decrease of cofilin phosphorylation, similar to PBDu (Fig 5H). When the phosphatase activity of slingshot was inhibited by Sennoside A[69], the level of cofilin phosphorylation increased under PDBu treatment. Also, the effect of A23187 on phospho-cofilin was counteracted by simultaneous treatment with Sennoside A, whereas phosphorylation of LIMK was unaffected by SSH inhibition, either with or without A23187 (Fig 5I). Consistently, podosome formation (after HT pressure stimulation) was blocked after slingshot inhibition, while VSMC efficiently formed podosomes on all stiffnesses after ROCK inhibition with Y27632 (Fig 5J). Together these results suggest that hydrodynamic pressure and PDBu treatment are both acting on cofilin phosphorylation through calcium and slingshot phosphatase, while stiffness sensing is modulating cofilin phosphorylation through RhoA-ROCK and LIMK activity (Figure 6). Both together lead to a change in VSMC phenotype, podosome formation and extracellular matrix remodelling and ultimately will contribute to the disease progression.

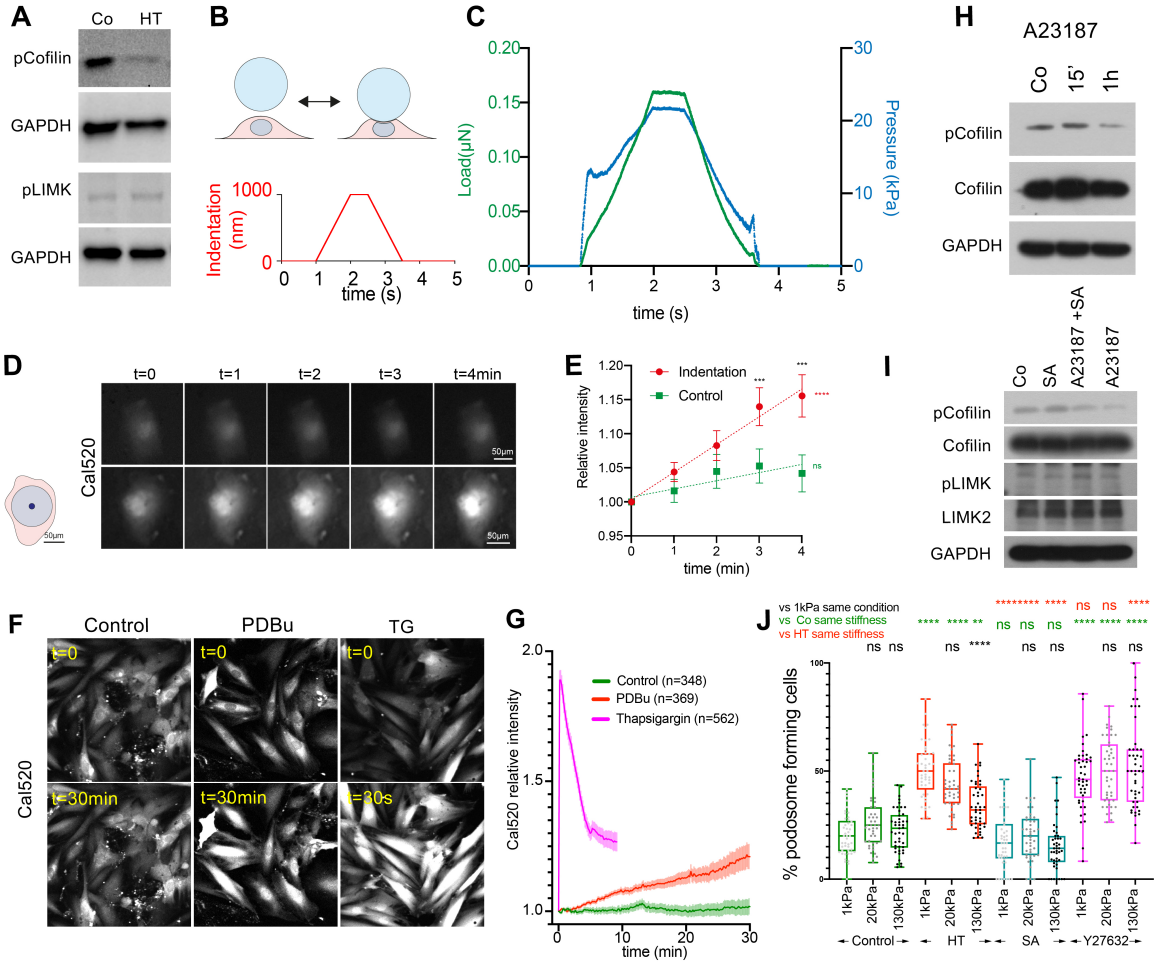

Figure 5: Pressure and PDBu stimulation induce calcium influx to regulate slingshot dependent cofilin phosphorylation. A) Hydrodynamic pressure stimulation reduces cofilin, but not LIMK phosphorylation. B) Schematic of pressure application with the nanoindenter (top) and indentation settings (bottom). A large diameter spherical tip is used to indent the cell with controlled pressure. C) example traces of corresponding load and pressure. Note that the initial large increase in load and pressure is due to the threshold load to find the cell surface. D,E) Indentation leads to a consistent increase in Cal520 intensity, while control cells do not show changes. Schematic on left indicates size of bead (in blue) and contact area at 1µm indentation (in dark blue) in comparison to cell area (in pink). E) Quantification of n=15 indented and 10 control cells (located nearby the indented cells) from 3 independent experiments. Error bars: SD; F,G) PDBu treatment leads to a consistent slow increase in Cal520 intensity, while thapsigargin (TG) induces a fast release of calcium from intracellular calcium stores. Note: lower panel shows 30 minute time point for Control and PDBu, but 30 second time point for TG; G) Quantification of n=348, 369 and 562 cells for control, PDBu and TG treatment. H) A23187 reduces cofilin phosphorylation after 1h. I) SSH inhibition increases cofilin phosphorylation after PDBu treatment and the reduction in pCofilin after A23187 is counteracted by simultaneous SSH treatment. J) SSH inhibition blocks podosome formation after hydrodynamic pressure stimulation on all stiffnesses, while ROCK inhibition enhances podosome formation after hydrodynamic pressure stimulation on all stiffnesses to a level otherwise seen on compliant surfaces only. *p < 0.0332; **p < 0.0021; ***p < 0.0002; ****p < 0.0001; ns, not significant; p-values from one-way ANOVA and Tukey test for multiple comparisons or t-test (E); E) Black asterisks represent comparison for single timepoints and different conditions, green and red asterisks represent p-values from linear regression and test for deviation from zero. J: green asterisks represent comparison to the controls of same stiffness group, green asterisks represent comparison to the HT condition of same stiffness, black asterisks to 1kPa of same treatment group. Box plots are displayed as median, upper and lower quartile (box) and range (whiskers).

Discussion

Atherosclerosis is a severe cardiovascular disease. Mechanical stimuli have been strongly implicated in both disease onset and progression. The role of wall stress on endothelial cells is well documented and determines atheroprone and atheroprotective regions[6-9]. Additionally,

ageing (and associated changes to the mechanical properties of the arterial wall) and hypertension are major risk factors[1-5, 38]. These mechanical stimuli affect also the sub-endothelial intima layer of the arterial wall and the residing vascular smooth muscle cells (VSMCs), which are critically involved in the early stages of atherosclerosis[12]. However, the effect of the different overlapping physiological or pathological mechanical stimuli on intimal VSMCs are still unclear.

Here we show that two mechanical stimuli, when combined, compliance (mimicking the intima and especially pre-atherosclerotic lesions or atherosclerotic plaques), and hypertensive pressure led to a phenotypic switch of VSMCs.

Certain effects on cell morphology or actin stress fibres are stimulated by the hypertensive pressure alone or chemical stimuli (from ECs), suggesting a partial phenotypic change can be induced through these stimuli. However, a complete phenotypic switching including formation of podosomes and associated matrix degradation is strongly dependent on a combination of these stimuli with a compliant environment. The implication of this is significant for the processes seen during early atherosclerosis. The increased expression of non-collagenous extracellular matrix and associated inclusion of lipoproteins in the vessel wall during the early atherosclerotic phase further modifies the microscale stiffness[45], therefore, the combination of compliance with hypertensive pressure will enhance the phenotypic switch and accelerate matrix remodelling and atherosclerotic progression in a downward spiral.

It is important to mention that our findings are not contrasting the importance of endothelial mechanosensing in onset and progression of atherosclerosis. Endothelial cells determine the location of atheroprone regions[6-9, 11] while differences in haemodynamic pressure in different arteries do not correlate with the susceptibility to atherosclerosis. Brachial blood pressure is higher compared to aortic pressure due to pressure amplification in young humans (albeit not in old age), however atherosclerosis is most common and severe in the aorta, followed by femoral arteries[70, 71]. Rather, our data suggests that chemical signals sent from the endothelium can initiate the phenotypic switch in VSMCs through various chemical signalling pathways, including PDGF and Wnt pathways that activate PKC[11, 51, 52] and thus will affect calcium influx[68], cofilin phosphorylation[67] and podosome formation (Fig 5). Similarly, hypertension and atherosclerosis have been both linked to an upregulation of the vasoconstrictors Endothelin-1 [53] and Angiotensin II[54], which likewise lead to increased production of diacylglycerol and downstream activation of PKC [55] and indeed PKC is deregulated in atherosclerosis[72].

This shows that mechanical and chemical signals are not mutually exclusive but rather act together. Our findings suggest that pressure and rigidity sensing enhance the VSMC phenotypic switch and thus potentiate the cells effectiveness in remodelling the extracellular matrix. Similar to chemical stimulation, pressure can increase baseline calcium levels and therefore, hypertension might trigger or further speed up the disease progression. Rigidity sensing through the podosomes will in turn contribute to the remodelling of the pre-atherosclerotic lesions.

Importantly, we show that VSMCs podosomes are mechanosensitive and change their appearance, dynamics and function in a stiffness-dependent way. Mechanosensitive behaviour of podosomes was previously studied in monocytic cells, with differing outcomes. One study using dendritic cells on a fibrinogen matrix found an increase in podosome formation with increasing stiffness, while another study using macrophages found a higher degree of podosome formation on compliant fibronectin coated hydrogels [73, 74]. Similar to the latter study we find a larger degree of podosome formation on soft fibronectin, gelatin or collagen coated (not shown) surfaces. Moreover, we find changes to podosome dynamics, and their ability to degrade the extracellular matrix.

In addition to the role of substrate stiffness on podosome formation, several studies also investigated the force generation by podosomes. Podosomes produce forces through the actin core which are balanced with traction forces in the podosome ring[73, 75-77]. Forces were found to be oscillatory, with a two-mode oscillatory behaviour. A slower oscillating component indicated high mechanical activity lasting over time-periods in the range of 7 ±4 minutes[77]. Additionally, podosome forces display a fast oscillating component with a period of approx. 40s [73, 77], whereby the latter corresponded roughly also with oscillations in podosome stiffness, suggesting a correlation with actin turnover cycles [78]. We did not image the podosomes at high enough frame rates in order to identify the faster oscillation component in our cells. However, the longer oscillation period matched well with the fluctuating behaviour that we detected (Fig 2D). Our results suggest that the fluctuations can be explained by the dual activity of cofilin as nucleator and severing protein, depending on its (active) concentration[60, 61]. The active concentration of cofilin in turn depends on RhoA, which is activated in the vicinity of the podosome core in a contracyclical way compared to the actin assembly.

As the substrate stiffness orchestrates RhoA activity, the downstream pathway of ROCK and LIMK will affect cofilin phosphorylation and the overall propensity of cells to initiate podosome formation. Indeed, the level of RhoA-GTP is decreased on compliant surfaces, leading to the cofilin mediated actin nucleation and a larger fraction of cells forming podosomes after pressure or chemical stimulation[63, 79]. Moreover, once cells start forming podosomes, the regulation of RhoA-GTP level can locally form a feedback loop to dynamically modulate the cofilin activity and myosin-dependent oscillation (Fig 6B). The increase of RhoA-GTP level during the assembly phase of podosome can reduce the activity of cofilin in actin nucleation and lead to the subsequent podosome disassembly.
Previous work further showed that the force oscillations are consistent with the actin dependent oscillations of the podosome core and myosin dependent oscillations of the podosome ring[80]. Together with our findings, this suggests that stress or strain dependent effects might lead to the activation of RhoA and points towards a role for a negative regulator of RhoA activity in the podosome adhesion ring. At this moment we can only speculate about the upstream mechanosensor, but potential molecules include the RhoGAP DLC1 which interacts with talin[81-83]. DLC1 has been shown to bind to talin in a force dependent way as it interacts with the folded R8 domain only[81]. High enough strain on talin could therefore displace DLC1 from the unfolding R8 domain and remove its negative regulation of RhoA activity[81, 83]. Likewise, ARAP3, a dual GAP for RhoA and Arf, is dynamically recruited to the podosome in a FAK/PI3K-dependent manner[79]. Other BAR-domain containing RhoA GAPs , such as srGAP1, RICH1, and GMIP, are likely to sense the change of membrane curvature during the podosome formation (which we indeed detect even on glass coverslips, where podosomes appeared to lift the membrane upwards in their vicinity, Supplementary Figure S7)[84] and regulate local RhoA activity[85, 86]. However, future experiments need to untangle the stiffness dependent regulation of RhoA activation at the adhesion ring.

While the stiffness and pressure regimes used here were mimicking the human (patho-) physiology all experiments here were performed with A7r5 rat aortic vascular smooth muscle cells, a well-established cell line that has been used for many VSMC studies in the past. Using a cell line as opposed to primary cells allowed us to perform a large set of experiments needed to analyse the fundamental regulatory mechanisms of VSMC phenotypic switching. Importantly, experiments performed in primary human cells support the key findings of a regulation of podosome formation through pressure and stiffness and will be disseminated elsewhere.

Overall, our findings suggest a regulation of VSMC phenotypic switching through combined mechanical signalling through hemodynamic pressure and extracellular matrix stiffness, which could be targeted to mitigate early atherosclerotic processes and abate disease progression.

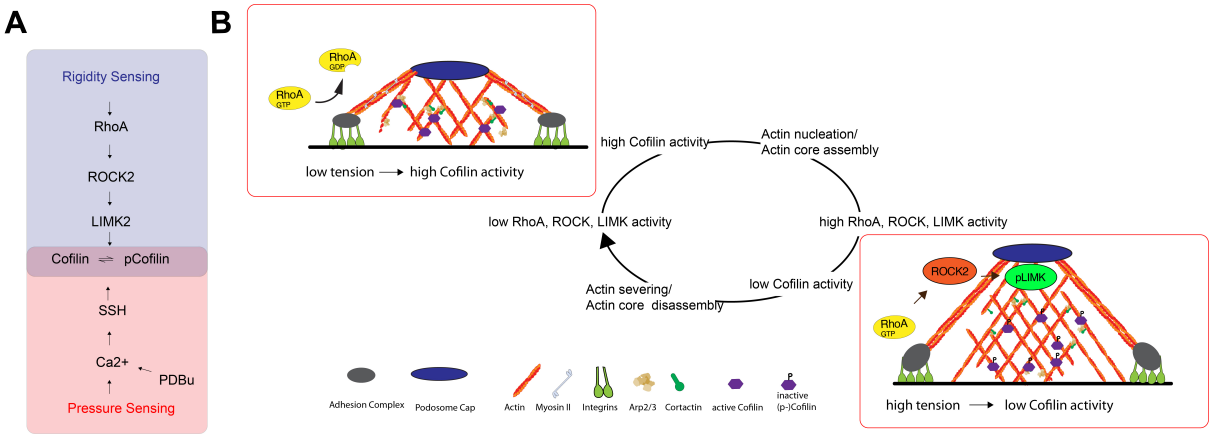

Figure 6: Schematic summarizing the pressure and stiffness dependent formation of podosomes in VSMCs. A) Pressure and PDBu signal through Ca2+ and SSH, while rigidity sensing acts through RhoA, ROCK2 an LIMK2 to modulate cofilin phosphorylation. B) Because cofilin switches between nucleation and severing depending on the concentration[60, 61], fluctuations in cofilin activity lead to a cyclic nature of podosome formation: high cofilin activity will lead to actin nucleation and actin core assembly of podosomes, which eventually invokes RhoA activation at the podosome ring (through a currently unknown mechanism), thereby increasing ROCK and LIMK activity. This in turn reduces the cofilin activity, leading to actin severing and actin core disassembly and a reduction in RhoA activity.

Methods

Antibodies and Reagents

Primary antibodies included vinculin (Sigma V9131, 1:200 for IF), cortactin (Sigma 4F11, 1:100 for IF), phospho-cofilin (Ser3) (CST 3311, 1:3000 for WB), cofilin (D3F9, CST 5175, 1:5000 for WB, 1:100 for IF), phospho-cortactin (Tyr421)(ThermoFisher 44854G, 1:1000 for WB), phospho-LIMK1 (Thr508)/LIMK2 (Thr505) (CST 3841, 1:1000 for WB), LIMK1 (CST #3842 or BD Biosciences # clone 42, 1:1000 for WB), LIMK2 (Abcam ab45165 or CST #8C11, 1:1000 for WB, 1:100 for IF), PAK1/2/3 (CST 2604, 1:1000 for WB), phospho-PAK1/2/3 (Thr402) (ThermoFisher PA1-4636, 1:1000 for WB), phospho-PAK4 (Ser474)/PAK5 (Ser602)/PAK6 (Ser560) (CST 3241, 1:1000 for WB), PAK4 (CST 62690 or 3242, 1:1000 for WB), ROCK2 (D1B1, CST 9029, 1:1000 for WB), ROCK1 (C8F7, CST 4035, 1:1000 for WB), β-tubulin (CST 2146, 1:3000 for WB), and GAPDH (ThermoFisher AM4300 or Abcam ab9485, 1:10000 for WB). Alexa Fluor 488 Phalloidin and Alexa Fluor 568 Phalloidin were from Invitrogen.

The following reagents were used at the specified concentrations after 24h serum starvation: Phorbol 12,13-dibutyrate (PDBu, Tocris #4153, 1µM), Thapsigargin (SCBT, sc-24017, 100nM), A23187 (SCBT, sc-3591, 1µM), SennosideA (Sigma 68909-5MG-F or Selleck #S4033, 10µM), Y27632 (Cambridge Bioscience or Selleck #S1049, 10 to 20µM), H1152 (Tocris #2414, 10µM), KD025 (Selleck #S7936, 10µM), ML141 (Selleck #S7686, 10µM), and A23187 (Selleck #S7778).

Plasmids:

Cofilin WT, cofilin S3A and cofilin S3E-pmiRFP were created by subcloning the respective cofilin constructs from pEGFP-N1 human cofilin plasmids using HindIII-HF and XmaI restriction sites.
pEGFP-N1 human cofilin WT, cofilin S3A and cofilin S3E were a gift from James Bamburg (Addgene plasmids # 50859, 50860 & 50861)[87]. pmiRFP703-N1 and pLifeAct-miRFP703 were a gift from Vladislav Verkhusha (Addgene plasmid # 79988 & 79993)[88]. mEos2-Actin-7 was a gift from Michael Davidson (Addgene plasmid # 57339)[89]. GFP-ROCK2 was a gift from Alpha Yap (Addgene plasmid # 101296)[90]. pLKO.1 - TRC cloning vector was a gift from David Root (Addgene plasmid # 10878)[91]. Tractin-tomato and tractin-GFP[92] were a gift from from M. Schell. The RhoA-FRET biosensor was a gift from Oliver Pertz[93]. mTFP-TRAF-Venus and mTFP-5AA-Venus were a gift from Nicolas Borghi[94]. Vinculin-mTFP and Vinculin-Venus were a gift from Carsten Grashoff [95].

shRNA:
The following sequences, inserted into an empty pLKO.1-TRC vector, were used for shRNA knockdowns: shScramble: 5'-CCTAAGGTTAAGTCGCCCTCG-3'; shROCK1#1 5'-GGTTTATGCTATGAAGCTTCT-3'; shROCK1#2 5'-GCATTTGCCAATAGTCCTTGG-3'; shROCK1#3: 5'-GCCGACTTTGGTACTTGTATG-3'; shROCK1#4: 5'- GCACCAGTTGTG CCTGATTTA -3'; shROCK2#1: 5'-TGCAAAGTTTATTATGATATA-3'; shROCK2#2: 5'-AACGTGGAAAGCCTGCTGGAT-3'; shROCK2#3: 5'-GCAGAAAGTTCCAAACAGA-3'; shROCK2#4: 5'-GTAGAAACCTTCCCAATTC-3'; shLIMK1#1 " 5'-CCTCCATTCGATGAACATCAT-3'; shLIMK1#2: 5'-AAGACTTGCGTAGCCTTAAGA-3'; shLIMK1#3: 5'-AATGCAGACCCTGACTATCTG-3'; shLIMK2#1: 5'-AATGGCAAGAGCTACGATGAG-3'; shLIMK2#2: 5'-AACAACCGAAATGCCATCCAC-3'; shLIMK2#3: 5'-GCCATCAAGGTGACTCACAAA-3'; all shRNA oligos were from Integrated DNA Technologies IDT. Cells were transfected with shRNAs for 96h before the experiments.

Cell culture, Immunostaining and Microscopy:
A7r5 rat atrial vascular smooth muscle cells were cultured in DMEM with 5% FBS, 1% Glutamax and 1% Penecillin/Streptamycin (P/S)). Cells were transfected using Lipofectamine LTX with plus reagent, following the manufacturer's instructions. For immunostaining, cells were fixed with 4% PFA for 10 minutes, permeabilized with 0.2% triton X-100 in PBS for 5 minutes, blocked with 5% BSA in PBS for 1h and stained in the antibody solutions in immunostaining buffer (20 mM Tris, 155 mM NaCl, 2 mM EGTA, 2 mM MgCl2, 1% BSA at pH 7.4) [96]. Cells were washed three times for 10 minutes with PBS after each step and mounted in MOWIOL 4-88 (0.1g/ml in Glycerol/Water/Tris (0.2M, pH8.0) at a ratio of 1/1/2) containing a final concentration of 4% n-propyl gallate. Live cell imaging was performed on an inverted Nikon Eclipse Ti-E microscope with a Nikon DS-Qi2 sCMOS camera (Podosome lifetime imaging) or a Nikon Ti2 SoRa spinning disc microscope with two Photometrics Prime BSI cameras for simultaneous imaging (FRET, Calcium imaging, used in confocal mode), both equipped with environmental chamber with temperature and CO_2 control. Podosome immunofluorescence imaging was performed on a or a Nikon Ti2 SoRa spinning disc microscope with a 60x 1.49NA objective in SoRa 4x magnification mode. Imaging of cells after pressure stimulation was done on a Leica DMI8 epifluorescence microscope with a Leica DFC9000 GT camera.
Fluorescence loss after photoconversion experiments were performed a Perkin Elmer UltraView VOX Spinning Disc Confocal. The photoconvertible mEos2-Actin was excited by an instant pulse of 405nm UV laser at cofilin-positive podosomes. The decay

phase of the photoconverted red mEos2-Actin was then imaged at the rate of 1 second per frame.

PDMS substrates

Flat PDMS substrates were prepared as described previously[97]. Briefly, Sylgard 184, Sylard 527 or mixtures at the Ratios of 1:5, 1:10 and 1:20 were spin coated with a 150i spin processor (SPS), onto coverslips. Before spin coating, Sylgard 527 was pre-cured at 70ºC for 30 minutes with intermitted mixing to achieve a comparable viscosity to the Sylgard 184 mixture. The stiffness of mixtures was measured by Rheology as described previously[46]. PDMS substrates were coated with fibronectin, or DQ-gelatin for matrix degradation experiments.

Pressure stimulation

Hydrodynamic pressure stimulation was performed in a MechanoCulture TR stimulator, placed inside a tissue culture incubator. The stimulator was modified setup for low pressure stimulation in the range of (human) normal (NBP) and hypertensive blood pressure (HT) and perfusion ports to supply pre-saturated cell culture medium. Cells were stimulated with a sinusoid profile (stretch: 0.5s, duration: 1s, hold: 0s, recovery 0.5s) and alternating between set pressures of 16 (peak load) and 8kPa (pre-load) to reach a measured pressure profile of 120/60mmHg for normal blood pressure stimulation and between 26 and 16kPa for a measured pressure profile of 180/120mmHg for hypertensive pressure stimulation. Cyclic pressure stimulations were performed for 12h and static pressure stimulations (at peak pressure setting) were performed for 30minutes. Control cells were placed inside the stimulator without applying pressure.

Cell stretching

Cell stretching experiments were performed using a FlexCell-4000 setup. Cells were seeded onto BioFlex Collagen I plates at ~50% confluence for biaxial strain stimulation the following day. Cells were stretched using a sinusoid profile cycling between 0 and 5% or 0 and 10% strain. Unstretched control cells were seeded onto unstretched membranes in parallel, retained in TC incubator, and then fixed simultaneously once the experiment had finished.

Nanoindentation

Nanoindentation experiments were performed using an Optics11 Chiaro nanoindenter attached to a Leica DMI-8 microscope. Measurements were performed above the nucleus with a R=49µm, k=0.46N/m probe (contact area radius = 10µm; suitable for a stiffness range between approx. 0.5 and 80kPa). The Hertzian contact model was used to fit the data. The contact point was identified from a contact point fit of the data to 20% of the maximal load and used to subsequently fit the young's modulus using an indentation depth of 1µm.

Ca2+ measurements:

For Calcium measurements cells were plated on fibronectin coated PDMS coverslips and loaded with Cal520 AM (abcam, ab171868) according to the manufacturer's instructions. Cells were then treated with 1µM PDBu, or 1µM thapsigargin and imaged on a Nikon Ti2 SoRa spinning disc microscope in confocal mode (50µm pinhole) with a Plan Fluor 10x air objective. Untreated cells were used as a control. To measure the calcium response after pressure stimulation, controlled force was applied onto cells using a Chiaro nanoindenter with a R=49µm, k=0.46N/m probe, using an indentation depth of 1µm (equalling a contact area of 150µm2) with a maximum pressure of 24 ± 4.4kPa.

Gelatin degradation
DQ-Gelatin is a fluorogenic substrate which emits green light once degraded by matrix metalloproteinases and excited by 488λ. To build a thin layer of gelatin on PDMS, 25mm cover slips pre-coated with PDMS were treated with 18W air plasma for 1 minute and then immediately coated with 0.1% DQ-Gelatin solution (DQ-Gelatin From Pig Skin, Fluorescein Conjugate; D12054) at room temperature for 10 minutes in a light-protected sterilized hood. Excess gelatin solution was removed by PBS. A7r5 cells were seeded at ~50% confluence 1 day before the experiment (PDBu treatment of pressure stimulation). DQ-Gelatin degradation was quantified as mean intensity over cell area, after background subtraction.

Image analysis
Image segmentation was performed using CellProfiler, ImageJ (OrientationJ) and Matlab as described previously[98]. Additionally, we added actin segmentation to the CellProfiler pipeline and trained an Ilastik pixel classification to detect actin dots. The pixel classification was then performed on the segmented and cropped single cell images. All measurements were combined, and dimensionality reduction was performed in Matlab using the t-SNE algorithm. Cluster borders were drawn manually, and populations from each separate repeat were calculated. Additional cell morphological analysis was performed with the the visually-aided morpho-phenotyping image recognition "VAMPIRE" software[99].
For analysis of Fluorescence loss after photoconversion, mEos2-Actin intensity decay profiles of each podosome were measured by ImageJ and fitted into a one-phase decay curve.
FRET analysis was performed in ImageJ. First donor and acceptor bleed through were determined using Vinculin-mTFP and Vinculin-Venus constructs using the PixFRET plugin. Donor bleed through was best fit with a constant value and Acceptor bleed through was determined to be negligible. Movies were processed using imageJ macro, by subtracting the background from all channels, calculating the bleed through corrected donor image, subtracting the bleed through corrected donor image from the FRET image, and then normalizing this by the Donor intensity.

RhoGTP pull down
A7r5 cells were seeded on the newly prepared fibronectin-coated PDMS substrate with the defined stiffness for 48 hours and were then treated with 1μM of PBDu for two hours. To detect the RhoA-GTP level, cells lysates were prepared according to manufacturer's instructions (RhoA Pull-Down Activation Assay Biochem Kit; Cytoskeleton Inc., BK036). Specifically, lysates with 300μg protein were incubated with the Rhotekin-RBD containing agarose bead at 4°C on a rotator. Total RhoA in the cell lysate and activated form of Rho-GTP in the agarose bead were detected by Western blot.

Statistical analysis
Data sets were tested for normal distribution using the Shapiro–Wilk test. All statistic tests were performed with GraphPad Prism using either t-tests for two conditions, or one-way ANOVA and correction for multiple comparisons.

Author Contributions
BS, ZF, IX, EM, SZ and TI performed the experiments and analysed the data. GJ, CS, CHY and TI designed the study. CHY and TI supervised the work and wrote the manuscript.

Acknowledgments

We would especially like to acknowledge M. Schell for the Tractin plasmids, Oliver Pertz for the RhoA biosensor plasmids, Nicolas Borghi for the mTFP-TRAF-Venus and mTFP-5AA-Venus, and Carsten Grashoff for the Vinculin-mTFP and Vinculin-Venus plasmids. We would like to thank Pei-Hsun Wu and Dennis Wirtz for the GUI/code and help with the VAMPIRE tool.

References:

1. Franklin, S.S. *et al.* Hemodynamic patterns of age-related changes in blood pressure. The Framingham Heart Study. *Circulation* **96**, 308-315 (1997).
2. Sutton-Tyrrell, K. *et al.* Elevated aortic pulse wave velocity, a marker of arterial stiffness, predicts cardiovascular events in well-functioning older adults. *Circulation* **111**, 3384-3390 (2005).
3. Chae, C.U. *et al.* Increased pulse pressure and risk of heart failure in the elderly. *JAMA* **281**, 634-639 (1999).
4. Mitchell, G.F. *et al.* Pulse pressure and risk of new-onset atrial fibrillation. *JAMA* **297**, 709-715 (2007).
5. Zieman, S.J., Melenovsky, V. & Kass, D.A. Mechanisms, pathophysiology, and therapy of arterial stiffness. *Arterioscler Thromb Vasc Biol* **25**, 932-943 (2005).
6. Givens, C. & Tzima, E. Endothelial Mechanosignaling: Does One Sensor Fit All? *Antioxid Redox Signal* **25**, 373-388 (2016).
7. Mehta, V. *et al.* The guidance receptor plexin D1 is a mechanosensor in endothelial cells. *Nature* **578**, 290-295 (2020).
8. Xanthis, I. *et al.* beta1 integrin is a sensor of blood flow direction. *J Cell Sci* **132**, jcs229542 (2019).
9. Baeyens, N. *et al.* Syndecan 4 is required for endothelial alignment in flow and atheroprotective signaling. *Proc Natl Acad Sci U S A* **111**, 17308-17313 (2014).
10. Iskratsch, T., Wolfenson, H. & Sheetz, M.P. Appreciating force and shape-the rise of mechanotransduction in cell biology. *Nat Rev Mol Cell Biol* **15**, 825-833 (2014).
11. Li, M., Qian, M., Kyler, K. & Xu, J. Endothelial-Vascular Smooth Muscle Cells Interactions in Atherosclerosis. *Front Cardiovasc Med* **5**, 151 (2018).
12. Basatemur, G.L., Jorgensen, H.F., Clarke, M.C.H., Bennett, M.R. & Mallat, Z. Vascular smooth muscle cells in atherosclerosis. *Nat Rev Cardiol* **16**, 727-744 (2019).
13. Doran, A.C., Meller, N. & McNamara, C.A. Role of smooth muscle cells in the initiation and early progression of atherosclerosis. *Arterioscler Thromb Vasc Biol* **28**, 812-819 (2008).
14. Virmani, R., Kolodgie, F.D., Burke, A.P., Farb, A. & Schwartz, S.M. Lessons from sudden coronary death: a comprehensive morphological classification scheme for atherosclerotic lesions. *Arterioscler Thromb Vasc Biol* **20**, 1262-1275 (2000).
15. Jacobsen, K. *et al.* Diverse cellular architecture of atherosclerotic plaque derives from clonal expansion of a few medial SMCs. *JCI Insight* **2** (2017).
16. Chappell, J. *et al.* Extensive Proliferation of a Subset of Differentiated, yet Plastic, Medial Vascular Smooth Muscle Cells Contributes to Neointimal Formation in Mouse Injury and Atherosclerosis Models. *Circ Res* **119**, 1313-1323 (2016).
17. Talusan, P. *et al.* Analysis of intimal proteoglycans in atherosclerosis-prone and atherosclerosis-resistant human arteries by mass spectrometry. *Mol Cell Proteomics* **4**, 1350-1357 (2005).
18. Nakashima, Y., Wight, T.N. & Sueishi, K. Early atherosclerosis in humans: role of diffuse intimal thickening and extracellular matrix proteoglycans. *Cardiovasc Res* **79**, 14-23 (2008).
19. Langley, S.R. *et al.* Extracellular matrix proteomics identifies molecular signature of symptomatic carotid plaques. *J Clin Invest* **127**, 1546-1560 (2017).
20. Ang, A.H., Tachas, G., Campbell, J.H., Bateman, J.F. & Campbell, G.R. Collagen synthesis by cultured rabbit aortic smooth-muscle cells. Alteration with phenotype. *Biochem J* **265**, 461-469 (1990).

21. Little, P.J., Tannock, L., Olin, K.L., Chait, A. & Wight, T.N. Proteoglycans synthesized by arterial smooth muscle cells in the presence of transforming growth factor-beta1 exhibit increased binding to LDLs. *Arterioscler Thromb Vasc Biol* **22**, 55-60 (2002).
22. Lee, R.T. *et al.* Mechanical strain induces specific changes in the synthesis and organization of proteoglycans by vascular smooth muscle cells. *J Biol Chem* **276**, 13847-13851 (2001).
23. Stary, H.C. *et al.* A definition of initial, fatty streak, and intermediate lesions of atherosclerosis. A report from the Committee on Vascular Lesions of the Council on Arteriosclerosis, American Heart Association. *Arterioscler Thromb* **14**, 840-856 (1994).
24. Onoue, N. *et al.* Increased static pressure promotes migration of vascular smooth muscle cells: involvement of the Rho-kinase pathway. *J Cardiovasc Pharmacol* **51**, 55-61 (2008).
25. Kim, N.Y. *et al.* Biophysical induction of vascular smooth muscle cell podosomes. *PLoS One* **10**, e0119008 (2015).
26. Meinders, J.M., Kornet, L. & Hoeks, A.P. Assessment of spatial inhomogeneities in intima media thickness along an arterial segment using its dynamic behavior. *Am J Physiol Heart Circ Physiol* **285**, H384-391 (2003).
27. Rezvani-Sharif, A., Tafazzoli-Shadpour, M. & Avolio, A. Progressive changes of elastic moduli of arterial wall and atherosclerotic plaque components during plaque development in human coronary arteries. *Med Biol Eng Comput* **57**, 731-740 (2019).
28. Matsumoto, T., Goto, T., Furukawa, T. & Sato, M. Residual stress and strain in the lamellar unit of the porcine aorta: experiment and analysis. *J Biomech* **37**, 807-815 (2004).
29. Hemmasizadeh, A., Autieri, M. & Darvish, K. Multilayer material properties of aorta determined from nanoindentation tests. *J Mech Behav Biomed Mater* **15**, 199-207 (2012).
30. Claridge, M.W. *et al.* Measurement of arterial stiffness in subjects with vascular disease: Are vessel wall changes more sensitive than increase in intima-media thickness? *Atherosclerosis* **205**, 477-480 (2009).
31. Oie, T. *et al.* Local elasticity imaging of vascular tissues using a tactile mapping system. *J Artif Organs* **12**, 40-46 (2009).
32. Kohn, J.C., Lampi, M.C. & Reinhart-King, C.A. Age-related vascular stiffening: causes and consequences. *Front Genet* **6**, 112 (2015).
33. Sit, B., Gutmann, D. & Iskratsch, T. Costameres, dense plaques and podosomes: the cell matrix adhesions in cardiovascular mechanosensing. *J Muscle Res Cell Motil* **40**, 197-209 (2019).
34. Lakatta, E.G., Mitchell, J.H., Pomerance, A. & Rowe, G.G. Human aging: changes in structure and function. *J Am Coll Cardiol* **10**, 42A-47A (1987).
35. Laurent, S. *et al.* Aortic stiffness is an independent predictor of all-cause and cardiovascular mortality in hypertensive patients. *Hypertension* **37**, 1236-1241 (2001).
36. Gozna, E.R., Marble, A.E., Shaw, A.J. & Winter, D.A. Mechanical properties of the ascending thoracic aorta of man. *Cardiovasc Res* **7**, 261-265 (1973).
37. de Beaufort, H.W.L. *et al.* Comparative Analysis of Porcine and Human Thoracic Aortic Stiffness. *Eur J Vasc Endovasc Surg* **55**, 560-566 (2018).
38. Alexander, R.W. Theodore Cooper Memorial Lecture. Hypertension and the pathogenesis of atherosclerosis. Oxidative stress and the mediation of arterial inflammatory response: a new perspective. *Hypertension* **25**, 155-161 (1995).
39. Chouinard, J.A., Grenier, G., Khalil, A. & Vermette, P. Oxidized-LDL induce morphological changes and increase stiffness of endothelial cells. *Exp Cell Res* **314**, 3007-3016 (2008).
40. Oberleithner, H. *et al.* Differential action of steroid hormones on human endothelium. *J Cell Sci* **119**, 1926-1932 (2006).
41. Hochmuth, R.M. Micropipette aspiration of living cells. *J Biomech* **33**, 15-22 (2000).
42. Cuerrier, C.M., Gagner, A., Lebel, R., Gobeil, F., Jr. & Grandbois, M. Effect of thrombin and bradykinin on endothelial cell mechanical properties monitored through membrane deformation. *Journal of molecular recognition : JMR* **22**, 389-396 (2009).
43. Mathur, A.B., Collinsworth, A.M., Reichert, W.M., Kraus, W.E. & Truskey, G.A. Endothelial, cardiac muscle and skeletal muscle exhibit different viscous and elastic properties as determined by atomic force microscopy. *J Biomech* **34**, 1545-1553 (2001).

44. Vargas-Pinto, R., Gong, H., Vahabikashi, A. & Johnson, M. The effect of the endothelial cell cortex on atomic force microscopy measurements. *Biophys J* **105**, 300-309 (2013).
45. Tracqui, P. *et al.* Mapping elasticity moduli of atherosclerotic plaque in situ via atomic force microscopy. *J Struct Biol* **174**, 115-123 (2011).
46. Pandey, P. *et al.* Cardiomyocytes Sense Matrix Rigidity through a Combination of Muscle and Non-muscle Myosin Contractions. *Dev Cell* **44**, 326-336 e323 (2018).
47. Rezakhaniha, R. *et al.* Experimental investigation of collagen waviness and orientation in the arterial adventitia using confocal laser scanning microscopy. *Biomech Model Mechanobiol* **11**, 461-473 (2012).
48. Wu, P.H. *et al.* Single-cell morphology encodes metastatic potential. *Sci Adv* **6**, eaaw6938 (2020).
49. Deuschle, J.K. *et al.* In situ indentation testing of elastomers. *Acta Materialia* **56**, 4390-4401 (2008).
50. Johnston, I., McCluskey, D., Tan, C. & Tracey, M. Mechanical characterization of bulk Sylgard 184 for microfluidics and microengineering. *Journal of Micromechanics and Microengineering* **24**, 035017 (2014).
51. Moriya, S. *et al.* Platelet-derived growth factor activates protein kinase C epsilon through redundant and independent signaling pathways involving phospholipase C gamma or phosphatidylinositol 3-kinase. *Proc Natl Acad Sci U S A* **93**, 151-155 (1996).
52. Sheldahl, L.C., Park, M., Malbon, C.C. & Moon, R.T. Protein kinase C is differentially stimulated by Wnt and Frizzled homologs in a G-protein-dependent manner. *Curr Biol* **9**, 695-698 (1999).
53. Fan, J., Unoki, H., Iwasa, S. & Watanabe, T. Role of endothelin-1 in atherosclerosis. *Ann N Y Acad Sci* **902**, 84-93; discussion 93-84 (2000).
54. Kon, V. & Jabs, K. Angiotensin in atherosclerosis. *Curr Opin Nephrol Hypertens* **13**, 291-297 (2004).
55. Khalil, R.A. Protein Kinase C Inhibitors as Modulators of Vascular Function and their Application in Vascular Disease. *Pharmaceuticals (Basel)* **6**, 407-439 (2013).
56. Sakai, H., Kurihara, Y., Hashimoto, Y., Chiba, Y. & Misawa, M. Involvement of multiple PKC isoforms in phorbol 12,13-dibutyrate-induced contraction during high K(+) depolarization in bronchial smooth muscle of mice. *J Smooth Muscle Res* **46**, 225-233 (2010).
57. Wang, T., Kendig, D.M., Trappanese, D.M., Smolock, E.M. & Moreland, R.S. Phorbol 12,13-dibutyrate-induced, protein kinase C-mediated contraction of rabbit bladder smooth muscle. *Front Pharmacol* **2**, 83 (2012).
58. Kaverina, I., Stradal, T.E. & Gimona, M. Podosome formation in cultured A7r5 vascular smooth muscle cells requires Arp2/3-dependent de-novo actin polymerization at discrete microdomains. *J Cell Sci* **116**, 4915-4924 (2003).
59. Hai, C.M., Hahne, P., Harrington, E.O. & Gimona, M. Conventional protein kinase C mediates phorbol-dibutyrate-induced cytoskeletal remodeling in a7r5 smooth muscle cells. *Exp Cell Res* **280**, 64-74 (2002).
60. Wioland, H. *et al.* ADF/Cofilin Accelerates Actin Dynamics by Severing Filaments and Promoting Their Depolymerization at Both Ends. *Curr Biol* **27**, 1956-1967 e1957 (2017).
61. Andrianantoandro, E. & Pollard, T.D. Mechanism of actin filament turnover by severing and nucleation at different concentrations of ADF/cofilin. *Molecular cell* **24**, 13-23 (2006).
62. Bravo-Cordero, J.J., Magalhaes, M.A., Eddy, R.J., Hodgson, L. & Condeelis, J. Functions of cofilin in cell locomotion and invasion. *Nat Rev Mol Cell Biol* **14**, 405-415 (2013).
63. Rafiq, N.B.M. *et al.* A mechano-signalling network linking microtubules, myosin IIA filaments and integrin-based adhesions. *Nat Mater* **18**, 638-649 (2019).
64. Kelly, M.L. & Chernoff, J. Getting smart about p21-activated kinases. *Mol Cell Biol* **31**, 386-387 (2011).
65. Beech, D.J. & Kalli, A.C. Force Sensing by Piezo Channels in Cardiovascular Health and Disease. *Arterioscler Thromb Vasc Biol* **39**, 2228-2239 (2019).
66. Gilbert, G., Ducret, T., Marthan, R., Savineau, J.P. & Quignard, J.F. Stretch-induced Ca2+ signalling in vascular smooth muscle cells depends on Ca2+ store segregation. *Cardiovasc Res* **103**, 313-323 (2014).

67. Wang, Y., Shibasaki, F. & Mizuno, K. Calcium signal-induced cofilin dephosphorylation is mediated by Slingshot via calcineurin. *J Biol Chem* **280**, 12683-12689 (2005).
68. Lipp, P. & Reither, G. Protein kinase C: the "masters" of calcium and lipid. *Cold Spring Harb Perspect Biol* **3** (2011).
69. Lee, S.Y. *et al.* Identification of sennoside A as a novel inhibitor of the slingshot (SSH) family proteins related to cancer metastasis. *Pharmacol Res* **119**, 422-430 (2017).
70. Sawabe, M. *et al.* Sustained progression and loss of the gender-related difference in atherosclerosis in the very old: a pathological study of 1074 consecutive autopsy cases. *Atherosclerosis* **186**, 374-379 (2006).
71. McEniery, C.M. *et al.* Central pressure: variability and impact of cardiovascular risk factors: the Anglo-Cardiff Collaborative Trial II. *Hypertension* **51**, 1476-1482 (2008).
72. Fan, H.C., Fernandez-Hernando, C. & Lai, J.H. Protein kinase C isoforms in atherosclerosis: pro- or anti-inflammatory? *Biochem Pharmacol* **88**, 139-149 (2014).
73. Labernadie, A. *et al.* Protrusion force microscopy reveals oscillatory force generation and mechanosensing activity of human macrophage podosomes. *Nat Commun* **5**, 5343 (2014).
74. Mennens, S.F.B. *et al.* Substrate stiffness influences phenotype and function of human antigen-presenting dendritic cells. *Sci Rep* **7**, 17511 (2017).
75. Bouissou, A. *et al.* Podosome Force Generation Machinery: A Local Balance between Protrusion at the Core and Traction at the Ring. *ACS Nano* **11**, 4028-4040 (2017).
76. Glazier, R. *et al.* DNA mechanotechnology reveals that integrin receptors apply pN forces in podosomes on fluid substrates. *Nat Commun* **10**, 4507 (2019).
77. Dalaka, E. *et al.* Direct measurement of vertical forces shows correlation between mechanical activity and proteolytic ability of invadopodia. *Sci Adv* **6**, eaax6912 (2020).
78. Labernadie, A., Thibault, C., Vieu, C., Maridonneau-Parini, I. & Charriere, G.M. Dynamics of podosome stiffness revealed by atomic force microscopy. *Proc Natl Acad Sci U S A* **107**, 21016-21021 (2010).
79. Yu, C.H. *et al.* Integrin-matrix clusters form podosome-like adhesions in the absence of traction forces. *Cell Rep* **5**, 1456-1468 (2013).
80. van den Dries, K. *et al.* Interplay between myosin IIA-mediated contractility and actin network integrity orchestrates podosome composition and oscillations. *Nat Commun* **4**, 1412 (2013).
81. Haining, A.W.M. *et al.* Mechanotransduction in talin through the interaction of the R8 domain with DLC1. *PLoS Biol* **16**, e2005599 (2018).
82. Klapholz, B. & Brown, N.H. Talin - the master of integrin adhesions. *J Cell Sci* **130**, 2435-2446 (2017).
83. Yao, M. *et al.* The mechanical response of talin. *Nat Commun* **7**, 11966 (2016).
84. de Kreuk, B.J. & Hordijk, P.L. Control of Rho GTPase function by BAR-domains. *Small GTPases* **3**, 45-52 (2012).
85. Muller, P.M. *et al.* Systems analysis of RhoGEF and RhoGAP regulatory proteins reveals spatially organized RAC1 signalling from integrin adhesions. *Nat Cell Biol* **22**, 498-511 (2020).
86. Lawson, C.D. & Ridley, A.J. Rho GTPase signaling complexes in cell migration and invasion. *J Cell Biol* **217**, 447-457 (2018).
87. Garvalov, B.K. *et al.* Cdc42 regulates cofilin during the establishment of neuronal polarity. *J Neurosci* **27**, 13117-13129 (2007).
88. Shcherbakova, D.M. *et al.* Bright monomeric near-infrared fluorescent proteins as tags and biosensors for multiscale imaging. *Nat Commun* **7**, 12405 (2016).
89. Kanchanawong, P. *et al.* Nanoscale architecture of integrin-based cell adhesions. *Nature* **468**, 580-584 (2010).
90. Priya, R. *et al.* Feedback regulation through myosin II confers robustness on RhoA signalling at E-cadherin junctions. *Nat Cell Biol* **17**, 1282-1293 (2015).
91. Moffat, J. *et al.* A lentiviral RNAi library for human and mouse genes applied to an arrayed viral high-content screen. *Cell* **124**, 1283-1298 (2006).
92. Johnson, H.W. & Schell, M.J. Neuronal IP3 3-kinase is an F-actin-bundling protein: role in dendritic targeting and regulation of spine morphology. *Mol Biol Cell* **20**, 5166-5180 (2009).

93. Fritz, R.D. *et al.* A versatile toolkit to produce sensitive FRET biosensors to visualize signaling in time and space. *Sci Signal* **6**, rs12 (2013).
94. Borghi, N. *et al.* E-cadherin is under constitutive actomyosin-generated tension that is increased at cell-cell contacts upon externally applied stretch. *Proc Natl Acad Sci U S A* **109**, 12568-12573 (2012).
95. Grashoff, C. *et al.* Measuring mechanical tension across vinculin reveals regulation of focal adhesion dynamics. *Nature* **466**, 263-266 (2010).
96. Iskratsch, T. *et al.* Two distinct phosphorylation events govern the function of muscle FHOD3. *Cell Mol Life Sci* **70**, 893-908 (2013).
97. Tabdanov, E. *et al.* Micropatterning of TCR and LFA-1 ligands reveals complementary effects on cytoskeleton mechanics in T cells. *Integr Biol (Camb)* **7**, 1272-1284 (2015).
98. Pedrosa, A.R. *et al.* Tumor Angiogenesis Is Differentially Regulated by Phosphorylation of Endothelial Cell Focal Adhesion Kinase Tyrosines-397 and -861. *Cancer research* **79**, 4371-4386 (2019).
99. Wu, P.H. *et al.* Evolution of cellular morpho-phenotypes in cancer metastasis. *Sci Rep* **5**, 18437 (2015).